Subspace projection filters for imaging in random media

Liliana Borcea and George Papanicolaou and Chrysoula Tsogka

Subspace projection filters for imaging in random media

Liliana Borcea [a,1], George Papanicolaou [b,2], Chrysoula Tsogka [c,3]

[a] *Computational and Applied Mathematics, Rice University, MS 134, Houston, TX 77005-1892*
[b] *Mathematics, Stanford University, Stanford CA 94305*
[c] *Applied Mathematics, University of Crete and & IACM/FORTH, GR-71409 Heraklion, Greece*

Abstract

We consider the problem of selective imaging extended reflectors in cluttered media. We propose a random travel time model for simulating the array response matrix in clutter and we compare it with the full wave solution. Our simplified model captures very well the full wave random medium behavior as this is illustrated by our numerical results. The algorithm for selective array imaging uses coherent interferometry on a filtered version of the data. The filter, which is based on the singular value decomposition of the response matrix, enhances the signal reflected by the edges of the reflector. We illustrate the performance of the imaging algorithm with numerical simulations in the regime of ultrasonic non-destructive testing in concrete.

Key words: array imaging; random media; migration; coherent interferometry

1. Introduction

In many important applications, such as ultrasound medical imaging [18,19,20,21,27], foliage penetrating radar [22,30], land and shallow water mine detection [14], seismic inversion [3,16], etc., we seek to detect and image extended scatterers embedded in inhomogeneous media. We consider here broadband array imaging in the regime of ultrasonic non-destructive testing in concrete. A typical setup is shown schematically in Figure 1. The source at $\mathbf{x}_s$ emits a spherical wave and the time traces of the scattered echoes $\Pi(\mathbf{x}_r, \mathbf{x}_s, t)$ are recorded at the array receiver locations $\mathbf{x}_r$ in the array $\mathcal{A}$, for $r = 1, \ldots, N_r$, over

Email addresses: borcea@caam.rice.edu (Liliana Borcea), papanico@math.stanford.edu (George Papanicolaou), tsogka@tem.uoc.gr (Chrysoula Tsogka).

1 . The work of L. Borcea was partially supported by the ONR grant N00014-05-1-0699 and by the NSF grants DMS-0604008, DMS-0305056, DMS-0354658.

2 . The work of G. Papanicolaou was partially supported by US Army grant W911NF-07-2-0027-1, ONR grant N00014-02-1-0088, and AFOSR grant FA9550-08-1-0089.

3 . The work of C. Tsogka was partially supported by the European FP7 Marie Curie International Reintegration Grant MIRG-CT-2007-203438.

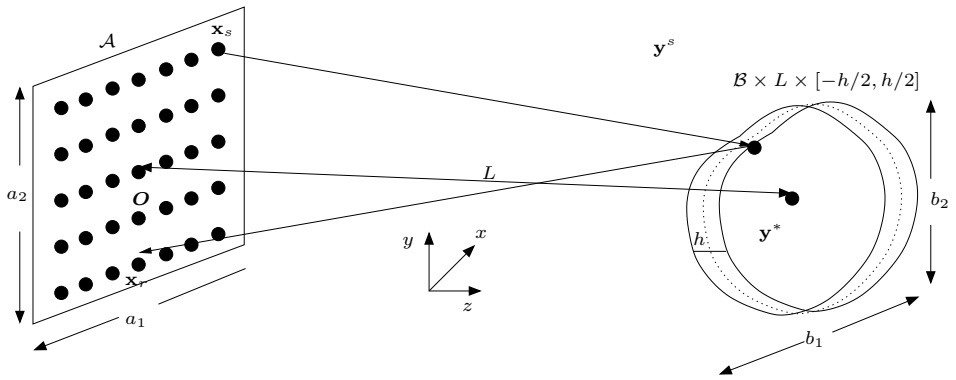

Figure 1. Schematic for array imaging an extended reflector.

some time window $t \in [0, T]$. Full array data are obtained by sending sequentially probing signals from N_s sources and recording in each case the traces $\Pi(\mathbf{x}_r, \mathbf{x}_s, t)$, $s = 1, ..., N_s$, $r = 1, ..., N_r$. The characteristic length scales of the problem, as illustrated in Figure 1, are the range L, the array aperture $\mathbf{a}$, the thickness h and the diameter $\mathbf{b}$ of the reflector.

The imaging problem that we address is to estimate the support of the reflector from the recorded traces. This can be done with higher accuracy if we recover information about the edges of the reflector, which are usually masked by the direct or specular reflections from the bulk of the object. A solution to this problem based on the singular value decomposition (SVD) of the response matrix frequency by frequency was proposed in [12]. In particular, it was shown that information about the edges is contained in the singular vectors for singular values that are intermediate between the large ones and zero. These transition singular vectors are associated with illuminating the edges of the object from sources at the edges of the array. Using such illumination for imaging with travel time migration gives selective imaging of the edges of the reflector.

In [12], the extended reflector was embedded in a homogeneous medium. We focus our attention here on imaging extended reflectors in cluttered media. By clutter we mean inhomogeneities in the medium that are unknown and cannot be estimated in detail. We model wave propagation in clutter with random travel times, assuming that rays do not bend significantly. This simplified model, which neglects the multiple scattering of the waves by the inhomogeneities, captures well the single scattering part of the wavefront. Numerical simulations show that for spectral characteristics of the response matrix there is good agreement between the simplified model and full wave simulations. These results are encouraging and suggest that we can rely on the simplified model for analyzing the performance of imaging algorithms in cluttered media.

Travel-time migration images in cluttered media are noisy and unstable. To stabilize the imaging process in clutter, we introduced in [6,8] the coherent interferometric (CINT) imaging functional which migrates cross-correlations of the traces over appropriate space-time windows [6,7,9]. The choice of the space-time windows depends on the clutter and it affects both the statistical stability and the resolution of the image. We showed in [7] that there is a trade-off between these two effects, and we introduced an adaptive algorithm for selecting the size of the space-time windows so as to achieve an optimal compromise between gaining statistical stability and losing resolution by blurring.

In this paper we first filter the data so as to enhance the signal reflected by the edges of the reflector and then we image with coherent interferometry to mitigate the effect of the clutter. This way we obtain selective and stable images of the edges of extended reflectors in cluttered media.

2. Imaging functionals

The travel-time (Kirchhoff) migration functional is given by [16,3]

$$\mathcal{I}^{\mathrm{KM}}(\mathbf{y}^s) = \int_{|\omega-\omega_0|\le B/2} d\omega \sum_{r=1}^{N} e^{-i\omega\tau(\mathbf{x}_r,\mathbf{y}^s)} \sum_{s=1}^{N} \widehat{\Pi}(\mathbf{x}_r,\mathbf{x}_s,\omega) e^{-i\omega\tau(\mathbf{x}_s,\mathbf{y}^s)}. \tag{1}$$

Here $\mathbf{y}^s$ is a search point in the region where we form the image and $\tau(\mathbf{x}_r,\mathbf{y}^s)$ is the travel time of the waves from the array element $\mathbf{x}_r$ to $\mathbf{y}^s$, in the background medium with sound speed c_0. For a constant c_0, $\tau(\mathbf{x}_r,\mathbf{y}^s) = |\mathbf{x}_r - \mathbf{y}^s|/c_0$. In general smooth media τ is given by Fermat's principle [13].

Travel-time migration of traces with significant delay spread due to multiple scattering in clutter produces images with speckles that are difficult to interpret. The images are also unstable, in the sense that they change unpredictably with the statistical realizations of the clutter. To stabilize the imaging process in clutter we introduced in [6,8,9] the coherent interferometry (CINT),

$$\begin{aligned}\mathcal{I}^{\mathrm{CINT}}(\mathbf{y}^s;\Omega_d,\kappa_d) = \int_{|\omega-\omega_0|\le \frac{B}{2}} d\omega \int_{|\omega'-\omega_0|\le \frac{B}{2},\ |\omega-\omega'|\le\Omega_d} d\omega' \sum_{r,r'\in\mathcal{X}\left(\frac{\omega+\omega'}{2},\kappa_d\right)} \\ \sum_{s,s'\in\mathcal{X}\left(\frac{\omega+\omega'}{2},\kappa_d\right)} \hat{Q}(\mathbf{x}_r,\mathbf{x}_s,\omega;\mathbf{y}^s)\overline{\hat{Q}(\mathbf{x}_{r'},\mathbf{x}_{s'},\omega';\mathbf{y}^s)},\end{aligned} \tag{2}$$

where the bar means complex conjugate and $\hat{Q}(\mathbf{x}_r,\mathbf{x}_s,\omega;\mathbf{y}^s)$ is the Fourier transform of the trace $\Pi(\mathbf{x}_r,\mathbf{x}_s,t)$ migrated to $\mathbf{y}^s$

$$\hat{Q}(\mathbf{x}_r,\mathbf{x}_s,\omega;\mathbf{y}^s) = \widehat{\Pi}(\mathbf{x}_r,\mathbf{x}_s,\omega) e^{-i\omega[\tau(\mathbf{x}_s,\mathbf{y}^s)+\tau(\mathbf{x}_r,\mathbf{y}^s)]}. \tag{3}$$

Here the set of indices in the summation is defined by

$$\mathcal{X}(\omega,\kappa_d) = \left\{ r,r' = 1,\ldots,N; \quad |\mathbf{x}_r - \mathbf{x}_{r'}| \le X_d(\omega) = \frac{c_0}{\omega\kappa_d} \right\}. \tag{4}$$

The key point in CINT is that instead of migrating the traces we migrate cross-correlations of the traces over appropriate space-time windows. The size of the space-time windows is critical, and depends on two intrinsic and characteristic parameters. These are the decoherence frequency Ω_d and the decoherence length X_d, i.e., the differences in frequencies and receiver locations, respectively, over which the traces become uncorrelated. The decoherence length $X_d(\omega)$, at frequency ω, is determined by the parameter κ_d as shown in (4).

In principle, κ_d and Ω_d could be estimated using statistical signal processing techniques, such as the variogram [15,26]. However, this estimation is very delicate and usually not sharp enough to give the best image. Instead, we proposed in [7] an adaptive estimation of κ_d and Ω_d that is coupled with the image formation process. Our algorithm determines κ_d and Ω_d so that there is an optimal trade-off between statistical stability and blurring.

Instead of working directly with the array data, $\widehat{\Pi}(\omega)$, as in the imaging functionals (1) and (2), we can work with a filtered version of the data $D[\widehat{\Pi}(\omega);\omega]$. In that case (1) becomes,

$$\mathcal{I}^{\mathrm{SM}}(\mathbf{y}^s) = \int_{|\omega-\omega_0|\le B/2} d\omega \sum_{r=1}^{N} e^{-i\omega\tau(\mathbf{x}_r,\mathbf{y}^s)} \sum_{s=1}^{N} \left(D[\widehat{\Pi}(\omega);\omega] \right)_{r,s} e^{-i\omega\tau(\mathbf{x}_s,\mathbf{y}^s)} \tag{5}$$

and is called subspace migration functional [12]. Similarly by replacing $\widehat{\Pi}(\omega)$ by $D[\widehat{\Pi}(\omega);\omega]$ in (3) we obtain the subspace coherent interferometric functional. Such filtered versions of the data were used for example in [10,12] and they are based on the singular value decomposition (SVD) of the response matrix,

$$\widehat{\Pi}(\omega) = \sum_{j=1}^{N} \sigma_j(\omega) \hat{\mathbf{u}}_j(\omega) \hat{\mathbf{v}}_j^*(\omega).$$

Here $\mathbf{u}_j$ and $\mathbf{v}_j$ are the left and right singular vectors of the response matrix and $\sigma_1(\omega) \geq \sigma_2(\omega) \geq, \ldots, \geq \sigma_N(\omega) \geq 0$ are its singular values. The filtered version of the response matrix, $D[\widehat{\Pi}(\omega); \omega]$, is defined in the following way,

$$D[\widehat{\Pi}(\omega); \omega] = \sum_{j=1}^{N} d_j(\omega) \sigma_j(\omega) \hat{\mathbf{u}}_j(\omega) \hat{\mathbf{v}}_j^*(\omega), \tag{6}$$

with $d_j(\omega) \geq 0$ the filter weights that we take as binary,

$$d_j(\omega) = \begin{cases} 1 & \text{if } j \in J(\omega) \\ 0 & \text{otherwise} , \end{cases} \tag{7}$$

for some set $J(\omega) \subset \{1, \ldots, N\}$ that determines which singular vectors of $\widehat{\Pi}(\omega)$ we keep. The simplest choice for the filter weights is to take $J^I(\omega) = \{1, 2, \ldots, N\}$ so that D becomes the identity. Another choice is to take $J^{detect}(\omega) = \{1\}$, i.e., keep the strongest reflection at each frequency. This is a very good method for detection because it is robust to noise. However, it is not a good method for imaging. That is because the largest singular vector corresponds in general to direct or specular reflections from the bulk of the object and imaging with it will not provide any information about the geometrical details of the object, such as the edges or the corners.

The filter $J^{detect}(\omega)$ is related to the DORT method [27] which is designed to selectively image or focus energy on well-separated point-like targets. It relies on the fact that the array response matrix for m such targets has rank m, and that each singular vector corresponds to a different target. For point-like targets that are not well separated, an optimization approach introduced in [10] can determine weights $d_j(\omega)$ that image the targets one by one in a robust way. This optimization approach is coupled with the adaptive CINT functional and therefore can be used in cluttered media. However, it does not generalize in an obvious way to extended reflectors.

To focus on the edges of an extended object we follow the approach in [12] and define the filter weights so that the normalized singular values $\sigma_j(\omega)/\sigma_1(\omega)$ of $\widehat{\Pi}(\omega)$ are in some interval $[a, b] \subset (0, 1)$,

$$J^{SM}(\omega; [a, b]) = \left\{ j \left| \frac{\sigma_j(\omega)}{\sigma_1(\omega)} \in [a, b] \right. \right\}. \tag{8}$$

Selectively imaging the edges of extended objects in homogeneous media with the subspace migration method was extensively studied in [12]. It was shown with numerical simulations that this imaging method masks the strong specular reflections from the bulk of the object and allows to image its edges quite effectively. It is also robust to noise for arrays that have a large number of sensors. The analysis of the imaging method was carried out in the Fraunhofer regime using the theory of generalized prolate spheroidal wave functions.

Here we will apply this method to selectively image the edges of a crack. This allows us to obtain a better estimate of its size especially in cluttered media. Numerical simulations using this approach are shown in Section 4.

3. Simulation setup and mathematical models

In this section we present the various numerical models that we use for simulating the array data. We consider three types of numerical simulations. In the first we compute the solution of the full wave

equation using a finite element time domain method. This can be applied both to homogeneous and cluttered media. It provides the more accurate solution, up to numerical errors, and is more expensive computationally. In the second type we use the linearized Born approximation to compute the field scattered by the reflector. In this case the computations are in the frequency domain and the background medium is homogeneous. A simple additive white noise model is used to simulate instrument noise. The third type is also a frequency domain computation based on the Born approximation. Here a random travel time model is used for computing an approximation of the background Green's function in clutter.

The numerical simulations are in two dimensions, in a regime that is often used in ultrasonic array imaging in concrete [24,25]. In this paper, elastic wave propagation in concrete is simplified to a scalar acoustic problem. Therefore, only pressure waves are considered and shear waves, Rayleigh waves, and mode conversion effects are neglected.

We solve the acoustic wave equation as a first order velocity-pressure system with the finite element, time domain method given in [2]. The setup is shown in Figures 2 and 3 for imaging in homogeneous and cluttered media, respectively. We simulate the wave propagation in an unbounded environment by surrounding the computational domain with a perfectly matched absorbing layer (PML), as shown in Figure 2.

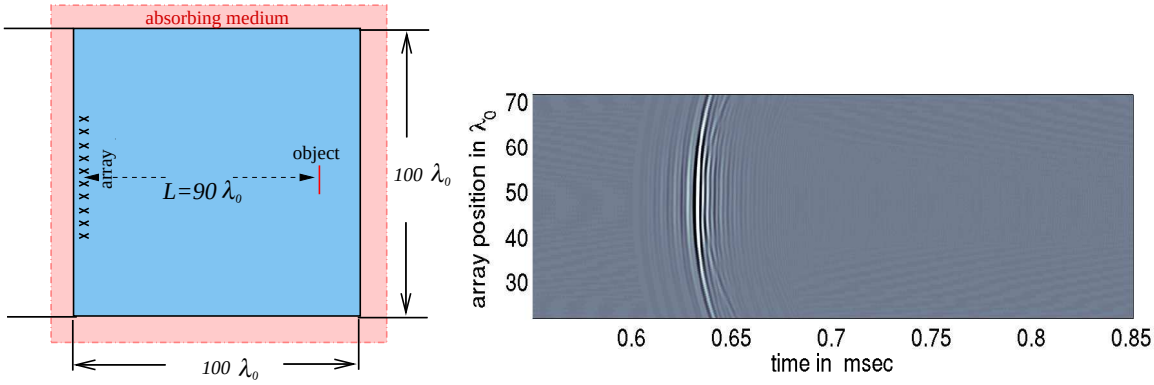

Figure 2. Schematic of array imaging in a homogeneous medium. The computational set-up is on the left. The traces received when illuminating from the central element in the array are on the right.

The array is linear with $N_r = N_s = 100$ transducers at a distance $h = \lambda_0/2$ from each other. The object to be imaged is a crack of length $12\lambda_0$ located at range $L = 90\lambda_0$ and at zero cross-range, measured with respect to the center of the array. We model it as a line segment on which the acoustic pressure field is zero. In the simulations we use the frequency band 150–450kHz, with bandwidth $B = 300$kHz. The reference sound speed is $c_0 = 3$km/s and therefore the wavelength at the central frequency $\omega_0 = 300$kHz is $\lambda_0 = 1$cm.

We model the clutter as a random process and we write the square of the index of refraction $n(\mathbf{x}) = c_0/c(\mathbf{x})$ as

$$n^2(\mathbf{x}) = n_0^2(\mathbf{x}) \left[1 + \sigma\nu\left(\frac{\mathbf{x}}{\ell}\right)\right]. \tag{9}$$

Here $n_0(\mathbf{x})$ is the smooth and known index of refraction of the background medium. We take $n_0(\mathbf{x}) = 1$ for simplicity, so that the wave speed $c(\mathbf{x})$ fluctuates about the constant value c_0. The normalized fluctuations are modeled by $\nu(\mathbf{x})$, which is a statistically homogeneous random process with mean zero and rapidly decaying correlation. The fluctuations have a characteristic length scale ℓ, the correlation length, which can be considered to be the typical size of the inhomogeneities. The parameter σ controls the strength of the fluctuations. The fluctuation process $\nu(\mathbf{x})$ is isotropic with Gaussian correlation

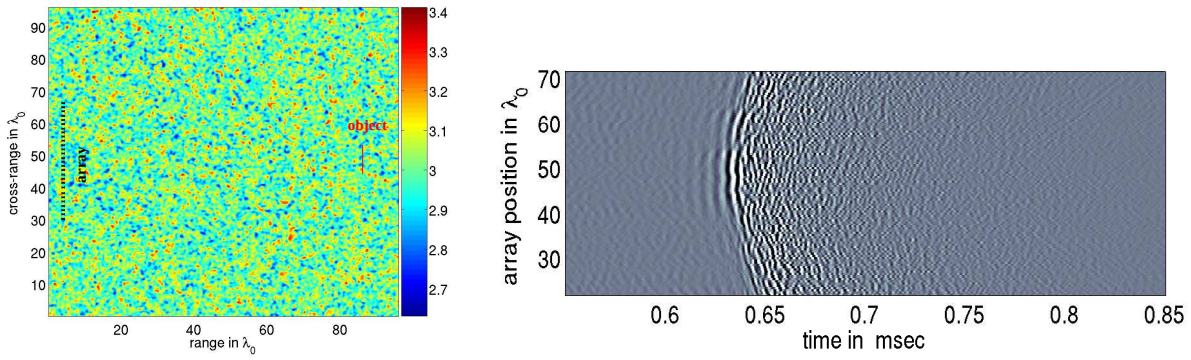

Figure 3. Array imaging in clutter. The computational set-up is shown on the left. The fluctuations in the sound speed are shown in color and the color-bar is in km/s. The traces received when illuminating from the central element in the array are on the right.

$$R(\mathbf{x},\mathbf{x}') = R\left(|\mathbf{x}-\mathbf{x}'|\right) = e^{-\frac{|\mathbf{x}-\mathbf{x}'|^2}{2\ell^2}}.$$

In the medium shown in Figure 3 we have $\ell = \lambda_0$ and $\sigma = 0.03$. Note that we are in a regime with small fluctuations $\sigma \ll 1$, as is expected in concrete structures. Nevertheless, because the range L is large with respect to λ_0 and ℓ, there is significant delay spread in the traces, as seen in Figure 3-right. The estimated transport mean free path [28,31] in the clutter is $75\lambda_0$. This is to be contrasted with the time reversal experiments in [17], where the range is about 10 transport mean free paths and all coherence is effectively lost in the echoes. Here the range L is comparable to the mean free path so there is some residual coherence in the data and coherent interferometric imaging can be effective.

Coherent imaging in strongly scattering media can be made effective by filtering prior to imaging the unwanted echoes that are due to the cluttered medium. We have analyzed two such filtering approaches: The first one distinguishes the echoes due to the reflector we wish to image from reflections due to layered interfaces using as tool the dependence of travel times on the offset between sources and receivers in the array. This filter, which can be applied only to layered media, annihilates single (primary) reflections at isolated, strong (layered) interfaces in a medium [4], as well as, the incoherent back-scattered field from random layering [5]. The second filtering approach is more general and can be applied to arbitrary cluttered media. The main idea is to identify the time windows that contain the coherent echoes from S by doing a spectral decomposition of the local cosine (LC) transform of the response matrix recorded at the array [1].

Simulation models based on the linearized Born approximation The simplest way for computing the scattered field by an object in a homogeneous medium is by using the linearized Born approximation [13] which neglects multiple scattering. Using this approximation we get the following expression for the response matrix,

$$\widehat{\Pi}(\mathbf{x}_r,\mathbf{x}_s,\omega) = k^2 \int d\mathbf{y}\rho(\mathbf{y})\hat{G}_0(\mathbf{x}_s,\mathbf{y},\omega)\hat{G}_0(\mathbf{x}_r,\mathbf{y},\omega). \tag{10}$$

In (10) the reflectivity $\rho(\mathbf{y})$ is assumed to be constant and equal to one on the crack and zero elsewhere and $\hat{G}_0$ is the free space Green's function

$$\hat{G}_0(\mathbf{x},\mathbf{y},\omega) = \frac{e^{\frac{i\omega|\mathbf{x}-\mathbf{y}|}{c_0}}}{4\pi|\mathbf{x}-\mathbf{y}|}. \tag{11}$$

The integral in (10) is evaluated with the mid-point rule which is equivalent to modeling the crack as a collection of points. In the computations we use 101 points placed uniformly, at distance $0.12\lambda_0$ apart. We generated data for $N_{freq} = 101$ equally spaced frequencies ω_i in the bandwidth, which are 30kHz apart.

To simulate instrument noise we added to $\widehat{\Pi}(\omega)$ a noise matrix $W(\omega) \in \mathbb{C}^{N_r \times N_s}$ with zero mean uncorrelated Gaussian distributed entries having variance ϵp. Here $\epsilon > 0$ and p is the average power received at the array per source, receiver and frequency

$$p = \frac{1}{N_r N_s N_{freq}} \sum_{i=1}^{N_{freq}} \left\| \widehat{\Pi}(\omega_i) \right\|_F ,$$

where $\| \cdot \|_F$ is the Frobenius matrix norm. The expected power of the noise $W(\omega)$ over all frequencies, receivers and sources is

$$\mathbb{E}\left[\sum_{i=1}^{N_{freq}} \|W(\omega_i)\|_F \right] = \epsilon N_r N_r N_{freq} p.$$

Since the total power of the signal received over all frequencies, receivers and sources is $N_r N_s N_{freq} p$, the signal to noise ratio (SNR) in dB is $-10 log_{10} \epsilon$.

Finally we used the following random travel time model which amounts to replacing in (10) the homogeneous Green's function by,

$$\hat{G}_\gamma(\mathbf{x}, \mathbf{y}, \omega) = \frac{e^{\frac{i\omega|\mathbf{x}-\mathbf{y}|(1+\gamma(\mathbf{x},\mathbf{y}))}{c_0}}}{4\pi|\mathbf{x}-\mathbf{y}|} \; ; \; \gamma(\mathbf{x}, \mathbf{y}) = \int_0^1 ds \; \nu\left(\frac{(1-s)\mathbf{x} + s\mathbf{y}}{l} \right). \tag{12}$$

Here ν are the normalized fluctuations as in (9). The model (12) can be derived by assuming that rays do not bend, i.e., by assuming that the ray between $\mathbf{x}$ and $\mathbf{y}$ is a straight line. This random travel time model is much simpler to implement and analyze than the full wave equation in random media. It does not model, however, the multiple scattering of the waves by the inhomogeneities of the medium and therefore there is no delay spread in the traces, as seen in Figure 4-bottom.

Simulated data sets We will show results for the following five data sets:

(i) *Homogeneous:* the response matrix is computed by solving the two-dimensional wave equation in a homogeneous medium with wave speed $c_0 = 3$km/s. The traces for the central source illumination are shown in Figure 2-right.

(ii) *Clutter:* the response matrix is computed by solving the two-dimensional wave equation in the realization of the random medium shown in Figure 3-left. The traces for the central source illumination are shown in Figure 2-right.

(iii) *Born with infinite SNR:* the response matrix is computed using the linearized Born model (10) with $\hat{G}_0$ given by (11) and infinite SNR (no additive noise). The traces for the central source illumination are shown in Figure 4-top left.

(iv) *Born with 0dB SNR:* in this case zero mean uncorrelated Gaussian noise $W(\omega)$ with variance p ($\epsilon = 1$) is added to the Born data. The traces for the central source illumination are shown in Figure 4-top right.

(v) *Random travel time model:* the response matrix is computed using the linearized Born model (10) with $\hat{G}_0$ replaced by G_γ defined in (12). The traces for the central source illumination are shown in Figure 4-bottom.

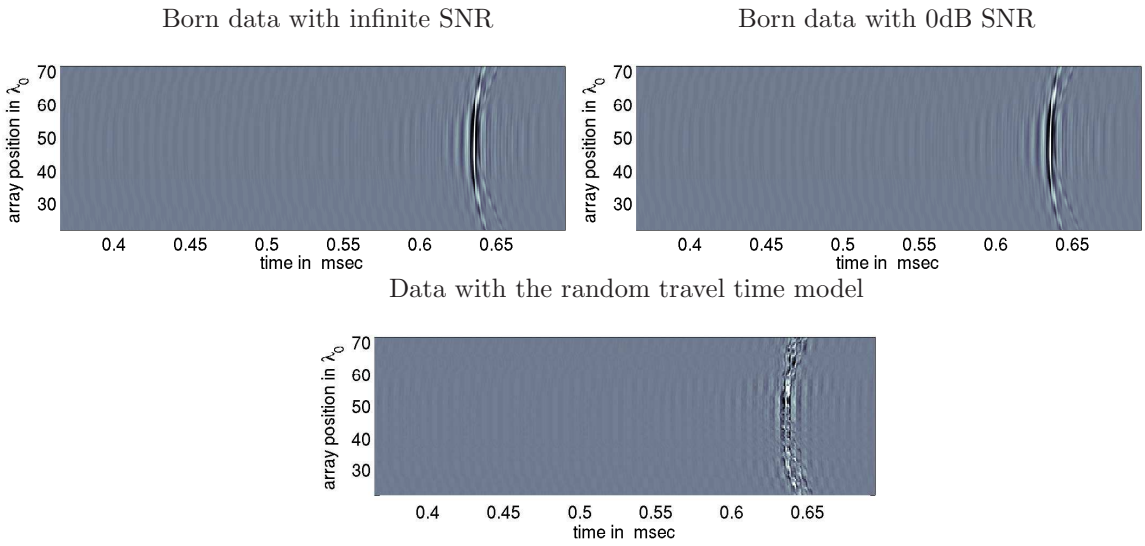

Figure 4. Traces on the array for the central source illumination. Top: the response matrix is simulated using the linearized Born model. Bottom: the random travel time model is used to simulate the response matrix.

Results on the singular value distribution of the response matrix

The problem of selective imaging extended reflectors in homogeneous media was considered in [11,12] in a so-called Fraunhofer diffraction regime. This regime is realized when we have very long distances of propagation, L, and arrays of large aperture, $\mathbf{a}$, when compared with the cross-range diameter, $\mathbf{b}$, of the reflectors. The reflectors are extended in the sense that $\mathbf{b}$ can be large with respect to the array spot size $(\lambda L)^2/|\mathcal{A}|$. One of the main results in [11,12] is that the linear (Born) approximation of the response matrix, $\hat{\Pi}(\omega)$, can be written in terms of a space and wave-number limiting Hilbert Schmidt operator. The properties of these operators are analyzed in detail in the work of Slepian, Landau and Pollack [23,29]. Using their results the following properties were obtained for the singular values and the singular vectors of the response matrix [12],

- The singular values of the response matrix, σ_j, are nearly constant for small j and plunge to zero at the critical index $n^\star = \left\lfloor \frac{|\mathcal{B}|}{(\lambda L)^2/|\mathcal{A}|} \right\rfloor$. This says that the effective rank of the response matrix is the number of spot sizes that fit in the object.
- The singular vectors corresponding to the leading singular values, define illuminations that return the strongest echoes to the array. The corresponding images are well concentrated inside the reflector. The opposite holds for singular vectors with index above the threshold n^*. Therefore, if we want singular vectors that peak on the edges of the reflector we should consider the plunge region, which corresponds to the intermediate singular values.

Next we look at the behavior of the singular values of the response for the five data sets described in Section 3. We will see that the numerical results are in excellent agreement with the theory. The corresponding imaging results are given in Section 4.

In Figure 5 we compare the normalized singular value distribution for the full wave data in the homogeneous medium and for the Born data. We consider three frequencies 200kHz, 300kHz and 400kHz. We note that the two curves are almost identical. Similar results are obtained for all frequencies in the bandwidth. We conclude that for this example the multiple scattering on the reflector does not play a significant role. We also observe in the plots the behavior predicted by the theory: the singular values are

constant at the beginning and then they plunge to zero at the critical value $N(\omega) = b/(\lambda L/a)$.

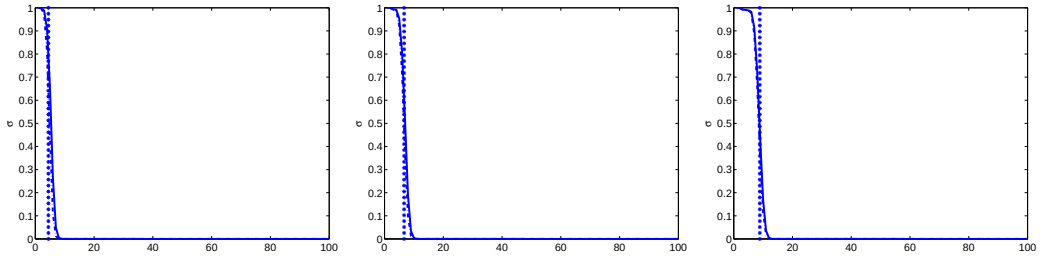

Figure 5. The normalized singular values of $\widehat{\Pi}(\omega)$ for the full wave data (continuous line) and the Born data (.− line) for frequencies 200kHz (left), 300kHz (middle) and 400kHz (right). The vertical line is the theoretical transition value $N(\omega) = b/(\lambda L/a)$ which is approximately 5, 7 and 9 respectively.

The effect of the different types of noise on the singular value distribution can be seen in Figure 6. On the left panel we observe that the additive Gaussian noise affects only the lower part of the spectrum. Therefore we expect that this type of noise will not have a significant impact on any of the imaging methods presented in Section 2. On the contrary, when the medium is cluttered the whole spectrum is affected as can be seen in the central and right panels of Figure 6. In this case we do not observe a plateau in the behavior of the singular values but a rather smoother transition to zero.

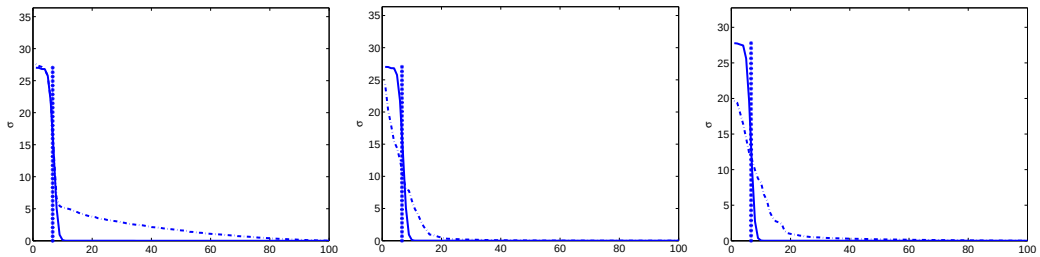

Figure 6. The singular values of $\widehat{\Pi}(\omega)$ at frequency 300kHz. Left: the continuous line is for the Born data with infinite SNR and the .− line is for the data with 0dB SNR. Middle: The continuous line is for the Born data with infinite SNR and the .− line is for the data obtained with the random travel time model. Right: The continuous line is for the homogeneous medium and .− line for the cluttered medium. The vertical line is the theoretical transition value $N(\omega) = \lfloor b/(\lambda L/a) \rfloor$ which is 7.

To better compare the singular value distribution between the random travel time model and the full wave solution in the cluttered medium we plotted the results for the two models in Figure 7. The two models present a similar behavior which is surprising at first because the random travel model completely neglects the multiple scattering of the waves by the inhomogeneities. This result is encouraging and suggests that we may be able to explain the spectral behavior of the response matrix in cluttered media using the simpler random travel time model. The analysis of this model although simpler is not straightforward and will be carried out in a forthcoming paper.

Finally we show in Figure 8 the first singular value of the response matrix as a function of frequency for the different data sets. In the results shown on the left panel we normalized the singular values by the maximal value of $\sigma_1(\omega)$ for the Born data with infinite SNR. In the results shown on the right panel we normalized the singular values by the maximal value of $\sigma_1(\omega)$ for the data in the homogeneous medium. We observe, as expected, that the additive Gaussian noise does not affect the largest singular value. Both for the random travel time model and the full wave solution in the cluttered medium we observe a decrease in the value of $\sigma_1(\omega)$ which expresses the fact that some energy is lost due to the scattering of the waves by the inhomogeneities.

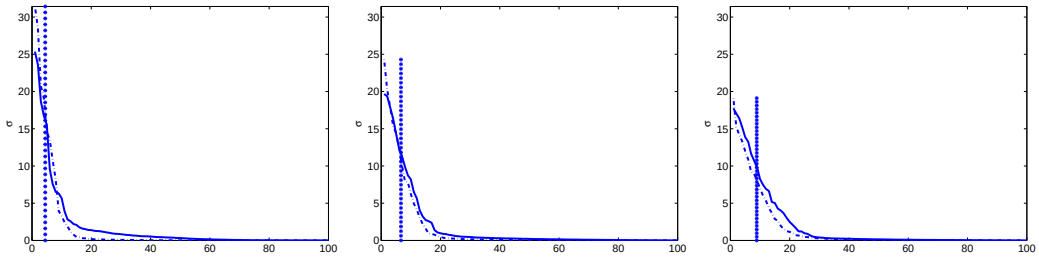

Figure 7. The singular values of $\widehat{\Pi}(\omega)$ for the cluttered medium (continuous line) and the random travel time model (.− line) for frequencies 200kHz (left), 300kHz (middle) and 400kHz (right). The vertical line in the figures is the theoretical transition value $N(\omega) = \lfloor b/(\lambda L/a) \rfloor$ which is 5, 7 and 9, respectively.

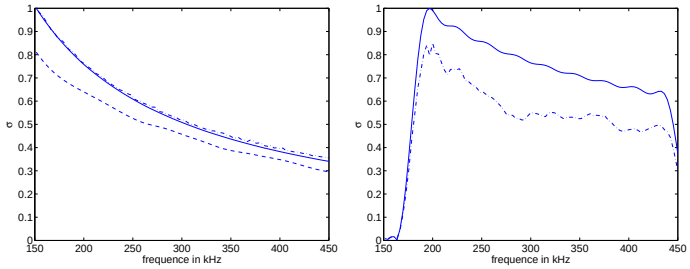

Figure 8. The largest singular values of the response matrix $\widehat{\Pi}(\omega)$ as a function of frequency. Left: the continuous line is for the Born data with infinite SNR, the .− line is for the data with 0dB SNR and the −− line is for the data obtained with the random travel time model. Right: The continuous line is for the homogeneous medium and the .− line for the cluttered medium.

Remark 1 In the numerical simulations the realization of ν in (12) is different than the one in (9).

4. Imaging results

In this section we show the subspace migration imaging results for the five data sets described in Section 3. We consider a search domain which is a rectangle of size $5\lambda_0 \times 20\lambda_0$ centered on the crack and the pixel size is $\lambda_0/2 \times \lambda_0/2$. In the images the true object is shown with a white line. In each of the following figures we show 4 panels, the left panel corresponds to keeping the normalized singular values which belong to the interval $[0.001, 1]$. This is a simple denoising approach as we neglect only the singular values which are below the noise level 0.001. The second panel corresponds to the detection method $J^{detect}(\omega) = \{1\}$. The other panels correspond to keeping the normalized singular values which belong to the some interval $[a, b]$ with the values of a and b defined in each figure.

First we show in Figure 9 the subspace migration imaging results for the Born data with infinite SNR. We observe that the whole crack is imaged when the whole spectrum is used (left panel) while only the central part of the crack is reconstructed when the first singular vector is used. By using the intervals $[0.001, 0.1]$ or $[0.1, 0.2]$ we obtain similar results which selectively image the tips of the crack. We can also use other intervals and the results remain the same as long as we stay away from 1. This is expected as the theory suggests that the information about the edges of the reflector is redundant. For the intervals $[0.001, 0.1]$ or $[0.1, 0.2]$ the imaging results are perfect even for the low SNR ratio as can be seen in the results of Figure 10. However, as we move to the lower part of the spectrum the images deteriorate. For the intervals $[0.001, 0.01]$ and $[0.001, 0.05]$ we observe that the focusing moves outside the object and the

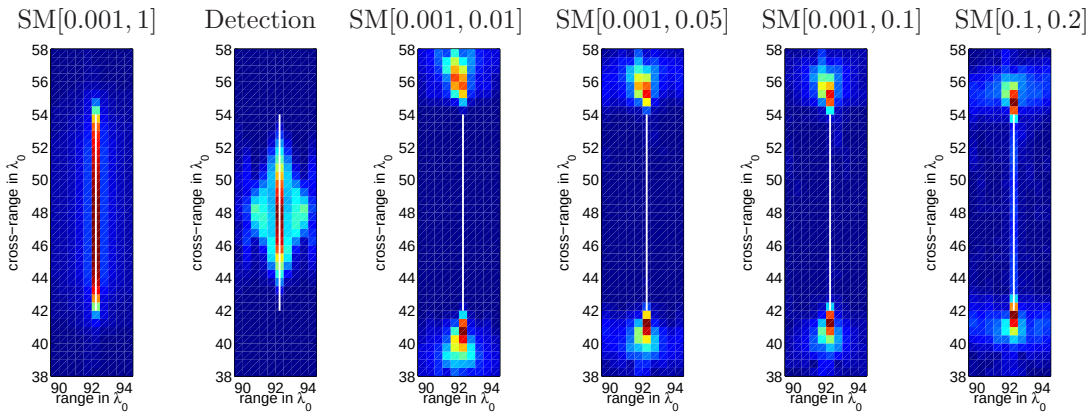

Figure 9. Subspace migration results for the Born data with infinite SNR.

image becomes corrupted by the noise for the low SNR data.

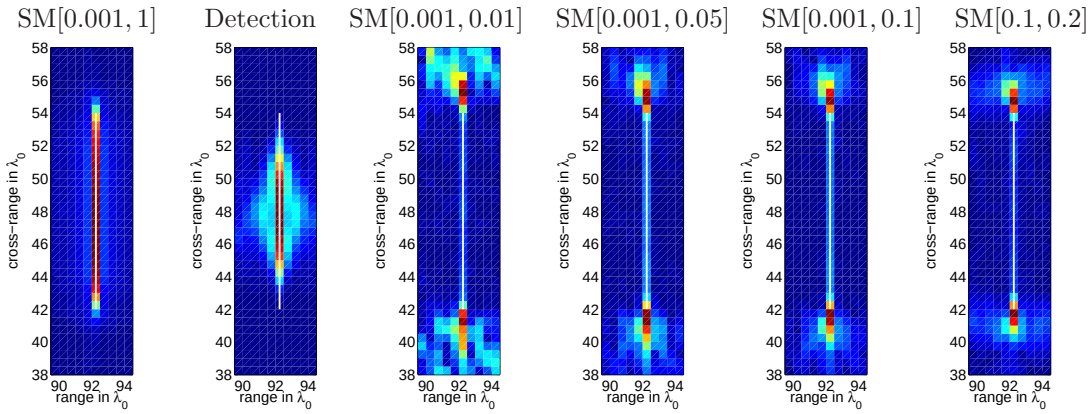

Figure 10. Subspace migration results for the Born data with 0dB SNR.

In Figure 11 we show the subspace migration results for the data obtained by solving the full wave equation in the homogeneous medium. We observe that there is no significant difference compared with the images obtained for the Born data shown in Figure 9.

The imaging results for the data obtained with the random travel time model are illustrated in Figure 12. The migration results shown on the top panels look quite noisy and the smoothing introduced by the coherent interferometric functional (2) is visible on the bottom panels of Figure 12. Here the decoherence parameters were obtained with the adaptive CINT approach [7] and are $\Omega_d = B/5$ and $\kappa_d = 0.12$.

Finally in Figure 13 we display the imaging results for the data obtained by solving the full wave equation in clutter. In this case the image changes significantly when we change the interval $[a, b]$ in which the normalized singular values belong (see third and fourth panels in Figure 13). In particular, selective imaging of the tips of the crack is achieved for intervals $[a, b]$ that are close to the value 0.4. We can also remark that the subspace migration images (top line of Figure 13) are more noisy than the corresponding ones for the random travel time model (see top line images of Figure 12). In this case coherent interferometry significantly improves the quality of the image as can be seen by the images in the bottom line of Figure 13. The decoherence parameters here are $\Omega_d = B/3$ and $\kappa_d = 0.12$.

Comparing Figures 12 and 13 we observe that the best imaging results for the random travel time data are obtained for the interval $[0.1, 0.2]$ while the interval $[0.4, 0.5]$ gives the best image for the full wave

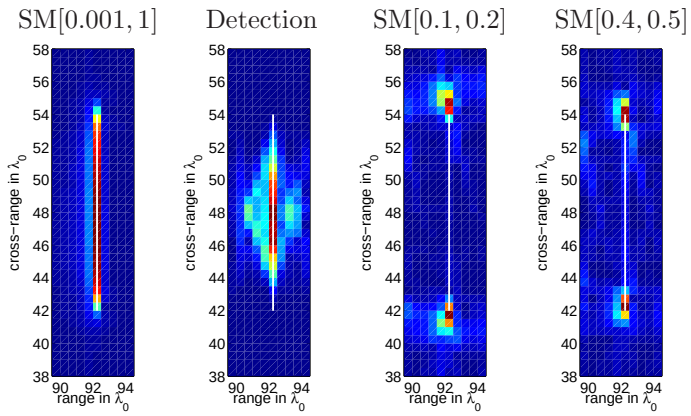

Figure 11. Subspace migration results for the data obtained by solving the full wave equation in a homogeneous medium.

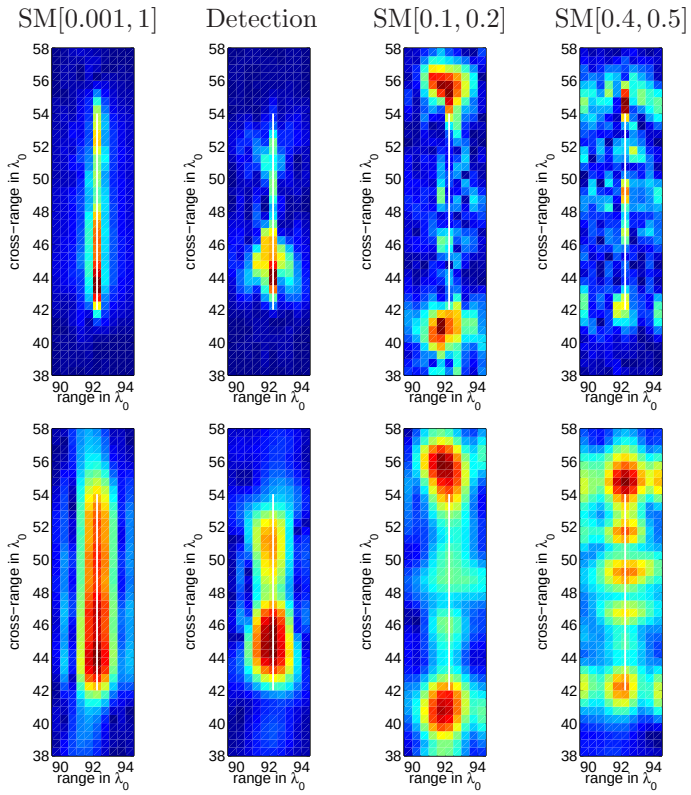

Figure 12. Imaging results for the data obtained with the random travel time model. Top line: the imaging method used is migration. Bottom line: the imaging method used is coherent interferometry.

data in clutter. This difference can be explained by the fact that the singular value curves for the random travel time model are below the curves for the full wave data in Figure 7. To better illustrate this we show in Figure 14 the normalized singular values of $\widehat{\Pi}(\omega)$ for the cluttered medium (continuous line) and the random travel time model (.− line) for the frequency of 400kHz. The vertical line corresponds to the 13-th normalized singular value which is about 0.2 for the random travel time model while it is about 0.4

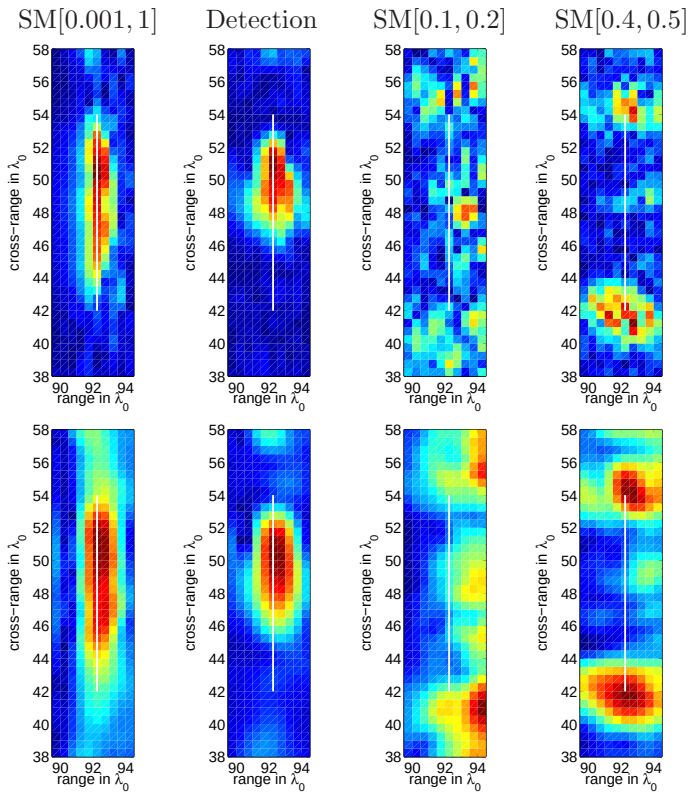

Figure 13. Imaging results for the data obtained by solving the full wave equation in the cluttered medium shown in the left panel of Figure 2. Top line: the imaging method used is migration. Bottom line: the imaging method used is coherent interferometry.

for the full wave data.

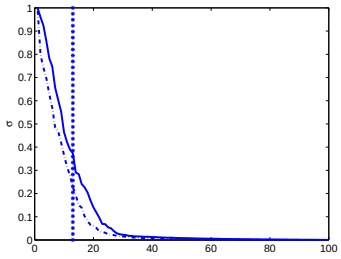

Figure 14. The normalized singular values of $\widehat{\Pi}(\omega)$ for the cluttered medium (continuous line) and the random travel time model (.− line) for the frequency of 400kHz. The vertical line corresponds to the 13-th normalized singular value.

5. Summary and conclusions

In this paper we addressed the problem of selective imaging of extended reflectors in cluttered media. We introduce a random travel time model for approximating the Green's function in clutter. Our numerical

results show that this simplified model captures well the behavior of wave propagation in random media as far as the imaging of edges is concerned. Edge enhancement in imaging is achieved with the use of a subspace projection filter which masks the strong reflections due to the bulk of the object. The imaging functional used is coherent interferometry, which is a smoothed version of travel time migration and gives statistically stable results in clutter. The effectiveness of the algorithm is illustrated with numerical simulations in the regime of ultrasonic non-destructive testing in concrete.

References

[1] R. Alonso, L. Borcea, G. Papanicolaou, and C. Tsogka. Detection and imaging in strongly backscattering randomly layered media. preprint, 2010.

[2] E. Bécache, P. Joly, and C. Tsogka. An analysis of new mixed finite elements for the approximation of wave propagation problems. *SIAM J. Numer. Anal.*, 37:1053–1084, 2000.

[3] N. Bleistein, J.K. Cohen, and J.W. Stockwell Jr. *Mathematics of multidimensional seismic imaging, migration, and inversion*. Springer, New York, 2001.

[4] L. Borcea, F. Gonzalez del Cueto, G. Papanicolaou, and C. Tsogka. Filtering deterministic layer effects in imaging. *SIAM Multiscale Model. Simul.*, 7:1267–1301, 2009.

[5] L. Borcea, F. Gonzalez del Cueto, G. Papanicolaou, and C. Tsogka. Filtering random layering effects in imaging. *SIAM Multiscale Model. Simul.*, 8:751–781, 2010.

[6] L. Borcea, G. Papanicolaou, and C. Tsogka. Interferometric array imaging in clutter. *Inverse Problems*, 21(4):1419–1460, 2005.

[7] L. Borcea, G. Papanicolaou, and C. Tsogka. Adaptive interferometric imaging in clutter and optimal illumination. *Inverse Problems*, 22(4):1405–1436, 2006.

[8] L. Borcea, G. Papanicolaou, and C. Tsogka. Coherent interferometric imaging. *Geophysics*, 71(4):SI165–SI175, 2006.

[9] L. Borcea, G. Papanicolaou, and C. Tsogka. Asymptotics for the space-time Wigner transform with applications to imaging. In P. H. Baxendale and S. V. Lototsky, editors, *Stochastic Differential Equations: Theory and Applications. Volume in Honor of Professor Boris L. Rozovskii*, volume 2 of *Interdisciplinary Mathematical Sciences*, pages 91–112. World Scientific, 2007.

[10] L. Borcea, G. Papanicolaou, and C. Tsogka. Optimal illumination and waveform design for imaging in random media. *J. Acoust. Soc. Am.*, 122:3507–3519, 2007.

[11] L. Borcea, G. Papanicolaou, and C. Tsogka. Optimal waveform design for array imaging. *Inverse Problems*, 23:1973–2020, 2007.

[12] Liliana Borcea, George Papanicolaou, and Fernando Guevara Vasquez. Edge illumination and imaging of extended reflectors. *SIAM Journal on Imaging Sciences*, 1(75-114), 2008.

[13] M. Born and E. Wolf. *Principles of optics*. Academic Press, New York, 1970.

[14] L. Carin, N. Geng, M. McClure, Y. Dong, Z. Liu, J. He, J. Sichina, M. Ressler, L. Nguyen, and A. Sullivan. Wide-area detection of land mines and unexploded ordnance. *Inverse Problems*, 18:575–609, 2002.

[15] G. Christakos. *Random field models in Earth Sciences*. Dover, New York, 2005.

[16] J. F. Claerbout. *Fundamentals of geophysical data processing : with applications to petroleum prospecting*. CA : Blackwell Scientific Publications, Palo Alto, 1985.

[17] A. Derode, A. Tourin, and M. Fink. Limits of time-reversal focusing through multiple scattering: Long range correlation. *J. Acoust. Soc. Am.*, 107:2987–2998, 2000.

[18] M. Fink. Time reversal mirrors. *J. Phys. D*, 26:1330–1350, 1993.

[19] M. Fink. Time reversed acoustics. *Physics Today*, pages 33–40, March 1997.

[20] M. Fink. Time-reversed acoustics. *Scientific American*, pages 91–97, November 1999.

[21] M. Fink, D. Cassereau, A. Derode, C. Prada, P. Roux, and M. Tanter. Time-reversed acoustics. *Rep. Prog. Phys.*, 63:1933–1994, 2000.

[22] A. Gustavsson, P. O. Frölind, H. Hellsten, T. Jonsson, B. Larsson, G. Stenström, and L. M. H Ulander. Development and operation of the foa carabas hf/vhf-sar system. In *Proc. 4th Int. Workshop on Radar Polarimetry*, Nantes, France, July 1998.

[23] H. J. Landau and H. O. Pollak. Prolate spheroidal wave functions, Fourier analysis and uncertainty, II. *Bell Systems Tech. J.*, 40:65–84, 1961.

[24] K.J. Langenberg, R. Marklein, K. Mayer, T. Krylov, P. Ampha, M. Krause, and D. Streicher. Wavefield inversion in nondestructive testing. In I. M. Pinto, V. Galdi, and L. B. Felsen, editors, *Electromagnetics in a Complex World - Challenges and Perspectives*, pages 277–285. Springer, 2003.

[25] R. Marklein, K.J. Langenberg, K. Mayer, J. Miao, A. Shilivinski, A. Zimmer, W. Müller, V. Schmitz, C. Kohl, and U. Mletzko. Recent applications and advances of numerical modeling and wavefield inversion in nondestructive testing. *Advances in Radio Science*, 3:167–174, 2005.

[26] G. Papanicolaou and K. Solna. Wavelet based estimation of kolmogorov turbulence. In P. Doukhan, G. Oppenmeim, and M. S. Taqqu, editors, *Long-Range Dependence: Theory and Applications*, pages 473–505. Birkhauser, 2003.

[27] C. Prada and M. Fink. Eigenmodes of the time reversal operator: A solution to selective focusing in multiple-target media. *Wave Motion*, 20:151–163, 1994.

[28] L. Ryzhik, G. Papanicolaou, and J. B. Keller. Transport equations for elastic and other waves in random media. *Wave Motion*, 24:327–370, 1996.

[29] D. Slepian and H. O. Pollak. Prolate spheroidal wave functions, Fourier analysis and uncertainty, I. *Bell Systems Tech. J.*, 40:43–64, 1961.

[30] L. M. H. Ulander and H. Hellsten. Low-frequency ultar-wideband array-antenna sar for stationary and moving target imaging. In *Conf. Proc. SPIE 13th Annual Int. Symp. on Aerosense*, Orlando, FL, April 1999.

[31] M. C. W. van Rossum and Th. M. Nieuwenhuizen. Multiple scattering of classical waves: microscopy, mesoscopy, and diffusion. *Reviews of Modern Physics*, 71:313–371, 1999.